

# Characterization of pathological stomach tissue using polarization-sensitive second harmonic generation microscopy

HWANHEE JEON, MACAULAY HARVEY, RICHARD CISEK,  ELISHA BENNETT, AND DANIELLE TOKARZ\* 

Department of Chemistry, Saint Mary's University, 923 Robie Street, Halifax, Nova Scotia, B3H 3C3, Canada

\*[danielle.tokarz@smu.ca](mailto:danielle.tokarz@smu.ca)

**Abstract:** Alterations in collagen ultrastructure between human gastric adenocarcinoma and normal gastric tissue were investigated using polarization-resolved second harmonic generation (PSHG) microscopy. Cylindrical and trigonal symmetries were assumed to extract quantitative PSHG parameters,  $\rho$ ,  $\kappa$  and  $S$ , from each image pixel. Statistically significant variations in these values were observed for gastric adenocarcinoma, indicating a higher disorder of collagen. Numerical focal volume simulations of crossing fibrils indicate increased  $S$  parameter is due to more intersecting collagen fibrils of varying diameters. These parameters were also able to distinguish between different grades of gastric adenocarcinoma indicating that PSHG may be useful for automated cancer diagnosis.

© 2023 Optica Publishing Group under the terms of the [Optica Open Access Publishing Agreement](#)

## 1. Introduction

Gastric cancer, also known as stomach cancer, is the third leading cause of cancer-related deaths among males worldwide [1]. In 2020 alone, an estimated 770 000 deaths globally were attributed to gastric cancer [2]. One of the reasons behind the high mortality rate is that patients are often diagnosed at an advanced stage since the disease is asymptomatic in its early stages [3]. Being diagnosed at the advanced stage leads to a poorer prognosis and a reduced survival rate [3].

The most common type of gastric cancer is gastric adenocarcinoma, representing 95% of cases [4]. It develops in gastric gland cells which play an essential role in the process of digestion. Gastric cancer diagnosis is typically confirmed by histological examination of stomach biopsies obtained using esophagogastroduodenoscopy, also known as upper endoscopy, followed by examination of stained biopsy or surgical resection tissue sections with hematoxylin and eosin dyes under bright-field microscopy by a pathologist. Examination of the adenocarcinoma cells in the tissue leads to differentiation into 3 classification levels: well differentiated (WDA), moderately differentiated (MDA) and poorly differentiated (PDA).

According to gastric cancer classification, a high degree of differentiation means that the cancer cells in the stomach tissue share many similar characteristics and organization with normal cells while a low degree of differentiation means that the cancer cells have lost their structural organization and share few features with normal cells [5]. For instance, cancer cells that are categorized as WDA display either subtle or no difference to normal cells [6] while cancer cells that are categorized as PDA can be easily distinguished because they have very little glandular formation, and they have a poorly cohesive structure [7]. Cancer cells with appearances that are different from WDA and PDA are characterized as MDA. These varying levels of differentiation are important prognostic indicators. A lower level of differentiation, such as PDA, is associated with a higher level of tumour aggressiveness and is more likely to spread quicker than the low-grade cancers while MDA and WDA are associated with intermediate and lower grade cancers, respectively [5].

About 75% of gastric cancers in Western populations are diagnosed as PDA [8]. This large percentage may be due to the ease in distinguishing poorly differentiated cancer cells from normal cells and the challenges experienced by pathologists in distinguishing well differentiated cancer cells. So, it's likely that many WDA and MDA patients are going misdiagnosed and therefore, methods to aid pathologists in diagnosing all three levels may prove particularly useful.

The stomach extracellular matrix (ECM) continually undergoes remodeling however, during cancer initiation and progression, the remodeling mechanism is disrupted resulting in abnormal changes to the structure and orientation of components in the ECM including the most abundant component of the ECM, collagen [9]. Therefore, cancer diagnostic accuracy could be improved by identifying and quantifying the disorganization of collagen. Since collagen in the ECM is primarily type I [10,11], it generates strong second harmonic generation (SHG) signals without staining [12]. As a result, several SHG techniques exist to distinguish differences in the ECM collagen structure within normal and cancerous tissues including the SHG signal intensity ratio obtained using forward and backward detection geometries [13–15], the structure tensor [16,17], texture analysis [18–21] and the Hough transform [22].

The polarization-resolved SHG (PSHG) signal in particular is very sensitive to the structure of the collagen assembly within the focal volume, hence, alterations in the ECM due to tumorigenesis should be detectable with the signal. The novelty of the technique is that PSHG measures disorder from the nanometer to focal volume scale using an optical microscope, requiring no special sample preparation, unlike other techniques that could interrogate samples at such scales, such as electron or X-ray microscopies, which are much more laborious to use for interrogating multiple samples. Therefore, PSHG microscopy is potentially a powerful tool for cancer diagnostics. Several forms of PSHG microscopy have been used to determine differences in the ECM collagen structure of cancerous tissue including polarization-in (PI) SHG microscopy [23–30], circular dichroism PI SHG microscopy [31,32], Stokes Mueller polarimetric SHG microscopy, double Stokes Mueller polarimetric SHG microscopy [33], polarization out (PO) SHG microscopy [34,35] and polarization-in, polarization-out (PIPO) SHG microscopy [19,33,36–39]. A comprehensive review of these techniques as they are related to the structure of ECM collagen in cancerous tissue can be found in [40,41].

Differences in ECM collagen structure within normal versus cancerous tissues have been observed using PSHG microscopy techniques in a variety of tissue cancer pathological samples, including breast cancer [25–27,29,33,42], ovarian cancer [15,31], bone cancer [43], colon cancer [29,44], lung cancer [19,39], melanoma [29], esophageal cancer [28], pancreatic cancer [37] and thyroid cancer [36,38]. In this study, PIPO SHG microscopy was used to investigate the difference in collagen structure PSHG parameters between PDA, MDA, WDA and their corresponding normal tissues. PIPO SHG microscopy was utilized as the microscope has a simpler detection geometry than Stokes Mueller and double Stokes Mueller polarimetric SHG microscopies however, it has a more advanced detection geometry than PI SHG and PO SHG with the presence of a polarization state generator and a polarization state analyzer allowing an additional dimensionality to the PSHG data which is thought to lead to more accurate fitting which is thought to lead to more accurate fitting. Furthermore, PIPO SHG microscopy provides the ability to extract several PSHG parameters in comparison to circular dichroism PI SHG microscopy. Specific PSHG parameters investigated included the cylindrical parameter,  $\rho$ , which has been previously related to the helical tilt of SHG emitters in collagen [45],  $\kappa$ , which has been related to the chiral structure of collagen fibers within a focal volume [46] as well as the trigonal parameter,  $S$ , which represents the balance between cylindrical and trigonal symmetries [25,26].

## 2. Materials and methods

### 2.1. Histology sample preparation

Tissue microarray microscope slides were purchased from SuperBioChips Laboratories (4F Cancer Research Institute Seoul National University, Korea). The slides contained two cores from each of 59 patients, with one core identified as gastric adenocarcinoma and the second as normal gastric tissue obtained adjacent to the cancer tissue for each patient. The tissue cores were 2.0 mm in diameter composed of formalin-fixed tissue specimens sectioned into 4  $\mu\text{m}$  thick slices and mounted on glass microscope slides. No histological stains were used. Of the 59 cores classified as cancerous, 41 were intact and gave sufficient SHG signal for imaging including 23 PDA, 10 MDA and 8 WDA. For the normal tissue cores, 37 were usable including 21 PDA, 8 MDA and 8 WDA. PSHG analysis was performed on 3-4 areas per core resulting in a total of 92, 40 and 32 PSHG scans for PDA, MDA and WDA, respectively, as well as 81, 28 and 31 PSHG scans for normal tissue adjacent to PDA, MDA and WDA, respectively.

### 2.2. Polarization-resolved SHG microscopy

The tissue was imaged with a custom PSHG microscope, schematically shown in Fig. 1, previously described [47]. Briefly, an ultrafast femtosecond duration pulsed laser (FemtoLux 3, EKSPLA) which operated with 5 MHz repetition rate and 290 fs duration pulses at a wavelength of 1030 nm was raster scanned across the tissue sample using a pair of galvanometric scanning mirrors (ScannerMAX, Pangolin Laser Systems). A polarization state generator (PSG) consisting of a stationary linear polarizer (LPVIS100, Thorlabs, Inc.) and a flat half-wave plate (MWPUM2-25-1030-V, Karl Lambrecht Corp.) in a motorized rotation mount was located before a 0.8 numerical aperture (NA) air immersion microscope objective (Plan-Apochromat 20x, Carl Zeiss AG) and was used for polarization control of the laser beam. The linear polarization state of the SHG signal was measured using a polarization state analyzer (PSA) consisting of an SHG polarizer (analyzer, LPVISA100, Thorlabs, Inc.) in a motorized rotation stage after a custom polarization independent 0.85 NA collection objective (Omex Technologies, Inc.). The SHG signal was collected in transmission mode using an interference filter centered at 515 nm with a 10 nm bandwidth (65-153, Edmund Optics, Inc.). SHG signal was measured using a single-photon-counting photomultiplier detector (H10682-210, Hamamatsu Photonics K.K.) and obtained using a data acquisition card (PCIe-6363, NI).

### 2.3. Polarization-resolved SHG image analysis

Polarization-dependent measurements of the SHG signal were carried out using the PIPO SHG technique as previously described [48]. The PIPO SHG technique involved collecting 65 images, each consisting of a sum of 100 individual frames with 6  $\mu\text{s}$  pixel dwell time and  $100 \times 100$  pixels. 65 images were obtained in total at each combination of 8 evenly spaced analyzer angles (0 to  $157.5^\circ$ ) for each of 8 evenly spaced half-wave plate angles (0 to  $78.75^\circ$ ), followed by one image taken at the same polarization parameters as the first image to verify that the tissue had not moved or burned, taking 14 minutes per PIPO SHG image stack. Any PIPO SHG data that had movement greater than 1 pixel was discarded.

To analyze data from the PIPO SHG technique, a laboratory Cartesian coordinate system, XYZ, was defined with respect to the principal propagation direction of the laser, Y, where XZ is the imaging plane (Fig. 1). Under the assumption that collagen fibers in tissue are cylindrically symmetric (equivalent to hexagonal symmetry in SHG) and the assumption that  $\chi_{XXZ}^{(2)} = \chi_{ZXX}^{(2)}$ , which is expected for rod-like structures [46,49], the SHG intensity ( $I_{2\omega}$ ) can be described as a function of the laser electric field polarization orientation from the Z-axis ( $\theta$ ), the orientation of the analyzer from the Z-axis ( $\varphi$ ), the average in-plane fiber orientation from the Z-axis ( $\delta$ ), and the second-order nonlinear optical susceptibility tensor components,  $\rho$  (equivalent to  $\chi_{ZZZ}^{(2)}/\chi_{ZXX}^{(2)}$ ),

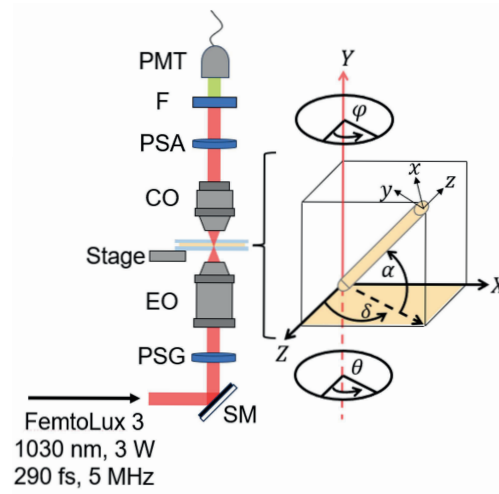


**Fig. 1.** A schematic diagram of the PIPO SHG microscope along with the coordinate systems used where a collagen fiber at an arbitrary orientation is represented as a yellow cylinder and the focal plane is the Z-X plane shown in yellow. The following abbreviations are used: SM - scanning mirrors, PSG - polarization state generator, EO - excitation objective, CO - collection objective, PSA - polarization state analyzer, F - optical filter, and PMT - photomultiplier tube detector.

which has been related to the helical angle of SHG emitters [45], and  $\kappa$  (equivalent to  $\chi_{XYZ}^{(2)}/\chi_{ZXX}^{(2)}$ ), which has been related to the nonlinear molecular chirality [46]:

$$I_{2\omega} = A|\rho \cos^2 \theta' \cos \varphi' + 2\kappa \sin \theta' \cos \theta' + \sin 2\theta' \sin \varphi' + \sin^2 \theta' \cos \varphi'|^2 + F \quad (1)$$

where  $\varphi' = \varphi - \delta$  and  $\theta' = \theta - \delta$ , while  $A$  and  $F$  were used to fit the amplitude and the noise, respectively. Note that in this study we neglect the contribution of circularly polarized light near the edge of the focal volume of our high numerical aperture objective [50]. We previously showed that PSHG values are altered at edges of a collagen fibril, hence, they are likely altered at tissue edges as well however, to observe the alteration, the pixel size was 180 nm, small enough so that just the more circular component of the high NA focal field is the dominant signal source. Since in the present study we used 1000 nm pixels, we believe the effect is averaged away because there are typically a large number of collagen fibrils within a single focal volume, and hence, a fibril is expected to be present near the center of the focal spot in most cases which will produce a dominant SHG signal as compared to fibrils near the edge. Therefore, gradients in the  $\rho$  values that result in single collagen fibrils due to circularly polarized light near the edge of the focal volume are not typically observed in collagenous tissues [50].

An additional quantification was performed using fitted pixel  $\rho$  values with a goodness of fit parameter  $R^2 \geq 0.8$ , by calculating the ratio of the number of pixels with  $\rho$  values between 2 and 3 per image to the total number of fitted pixels per image, termed the ratio of disordered pixels (RDP of  $\rho$ ) [51].

Analysis of the tissue PSHG data was also performed assuming trigonal ( $C_{3v}$ ) symmetry, which has a 3-fold symmetry axis and belongs to the hexagonal crystal system, similar to hexagonal symmetry, which has a 6-fold symmetry axis. Under the following simplifying assumption,  $\chi_{XXZ}^{(2)} = \chi_{ZXX}^{(2)}$ , the susceptibility tensor for trigonal symmetry contains all the terms for hexagonal symmetry, along with one additional term,  $\chi_{XXX}^{(2)}$  (see Supplement 1 for the derivation), giving the SHG intensity ( $I_{2\omega}$ ) that can be described by  $\theta$ ,  $\varphi$ ,  $\delta$ ,  $\rho$  and the trigonal parameter,  $S =$

$$\chi_{XXX}^{(2)} / \chi_{ZXX}^{(2)}:$$

$$I_{2\omega} = A[\rho \cos^2 \theta' \cos \varphi' + S \sin^2 \theta' \sin \varphi' + \sin 2\theta' \sin \varphi' + \sin^2 \theta' \cos \varphi']^2 + F \quad (2)$$

PIPO SHG analysis was performed by fitting the first 64 images using Eqs. (1) and (2). Although both  $\rho$  and  $S$  are extracted from Eq. (2) simultaneously, the  $\rho$  values used in our analysis were obtained from Eq. (1), for improved comparison with previous publications. Note that the differences in the  $\rho$  values between normal and cancerous tissues extracted from Eq. (2) demonstrated similar statistical significance to those obtained with Eq. (1), but had different absolute values.

In addition to obtaining the values of  $\rho$ ,  $\kappa$  and  $S$ , the degree of linear polarization (DOLP) was also determined using the following equation:

$$DOLP = \frac{\sqrt{s_1^2 + s_2^2}}{s_0} \quad (3)$$

where the polarization of the emitted SHG signal is described by the Stokes parameters,  $s_0$ ,  $s_1$  and  $s_2$  defined as:  $s_0 = I_{2\omega,0} + I_{2\omega,90}$ ,  $s_1 = I_{2\omega,0} - I_{2\omega,90}$  and  $s_2 = I_{2\omega,45} - I_{2\omega,-45}$  where  $I_{2\omega,a}$  is the SHG intensity at the analyzer angle  $a$ . An average DOLP is obtained by using Eq. (3) to calculate the DOLP at 8 incident laser polarizations ( $0^\circ$ ,  $22.5^\circ$ ,  $45^\circ$ ,  $67.5^\circ$ ,  $90^\circ$ ,  $112.5^\circ$ ,  $135^\circ$ , and  $157.5^\circ$ ), and for each one, two DOLP calculations were averaged, one using measurements at analyzer angles  $0^\circ$ ,  $45^\circ$ ,  $90^\circ$  and  $135^\circ$  and another at  $22.5^\circ$ ,  $67.5^\circ$ ,  $112.5^\circ$  and  $157.5^\circ$ . This was done because the SHG intensity decreases when the laser polarization orientation is  $90^\circ$  from the collagen axis resulting in noise dominating the SHG signal [36]. Therefore, to ensure a reliable DOLP measurement, all 16 independent DOLP measurements, which were already obtained from the PIPO SHG image stack, are averaged.

Custom MATLAB software (The Mathworks, Inc.) was used to fit the PIPO SHG data for each pixel without binning with Eqs. (1)–(3). The laser polarization state was measured to assess the influence of optical components. It was found that with a linearly polarized laser at  $\theta = 0^\circ$  and  $90^\circ$ , the DOLP of the laser traveling through both microscope objectives and a clean coverslip at the sample was measured to be 0.976 and 0.972 ( $\pm 0.001$ ), respectively, measured by a polarizer (LPVIS100, Thorlabs, Inc.) in a mechanical mount and a power meter. Further, birefringence was neglected, since the tissue sections were thin ( $< 5 \mu\text{m}$ ) [52].

#### 2.4. Numerical simulations

Numerical simulations were performed using an open-source program previously described [50,53]. The program calculates the SHG intensity as a result of the interaction between an electric field and a given spatial distribution of complex-valued second-order electric susceptibilities. The program assumes a perfectly collimated and polarized Gaussian ( $\text{TEM}_{00}$ ) laser beam incident on the back aperture of the microscope objective and computes the electric field within the focal volume. Then it computes the SHG field resulting from the interaction of the focal electric field with a given distribution of  $\chi^{(2)}$  tensors within the focal volume. The program then calculates the effect of the collection objective, to determine the SHG electric field distribution at the detection plane.

Two cylindrically symmetric structures were simulated with diameters of 200 and 340 nm, typical for collagen fibrils, and lengths much larger than the waist size of the laser focus. The cylindrically symmetric structures were oriented on adjacent optical planes, centered on the center of the focus, so that the two structures did not pass through each other. Simulations were performed where the  $\delta$  angle of the first fibril was held constant, and the  $\delta$  of the second fibril was varied between  $0^\circ$  and  $90^\circ$  in steps of  $10^\circ$ . The cylindrically symmetric structures were assigned

$C_{6v}$  symmetry  $\chi^{(2)}$  values with  $\chi_{zxx}^{(2)} = \chi_{xxz}^{(2)} = 1$ ,  $\chi_{zzz}^{(2)} = 1.9$ , and  $\chi_{xyz}^{(2)} = 0$ , hence,  $\rho = 1.9$  and  $\kappa = 0$ .

The numerical simulations were performed using a grid of  $100 \times 100 \times 59$  points (for  $X$ ,  $Z$  and  $Y$ ). Each voxel had a size of  $10 \times 10 \times 40.7$  nm. The NA values were assumed to be 0.8 for excitation and 0.85 for collection as in the PSHG microscope described in section 2.2. For all points within the focal volume, a refractive index of 1 was assumed. The effect of reflections from the fibrils were neglected due to limitations of the algorithm however, reflections and resultant quasi-phase matching should be considered in the future [54]. Additionally, the effect of reflections from coverslip interfaces were also neglected.

A simulated set of PIPO-SHG data for a single pixel with the cylindrically symmetric structures at a given position within the focal volume was achieved by running the program for all 64 combinations of laser polarization angles and analyzer angles performed in PIPO SHG measurements and fit using Eqs. (1) and (2).

### 3. Results

PIPO SHG microscopy was used to investigate the structural differences in the collagen present in poorly differentiated adenocarcinoma (PDA), moderately differentiated adenocarcinoma (MDA) and well differentiated adenocarcinoma (WDA) tissues versus normal gastric tissues in pathological tissue samples obtained from tumor adjacent tissues in patients diagnosed with these cancers, and results are presented in Fig. 2 and Table 1. Normalized SHG intensity images of typical regions of interest are shown in Fig. 2 panels a1-a6, obtained by summing 64 polarization-dependent images from each PIPO SHG scan and applying a logarithmic scale. They visualize ECM collagen content in normal (columns 1-3) and cancerous (columns 4-6) samples of stomach. Color-coded maps of the corresponding fitted  $\rho$  values for each pixel are shown in Fig. 2 panels b1-b6. They represent the level of organization of collagen within the tissue. Regions with  $\rho$  values close to 3 represent low levels of organization while regions with  $\rho$  values lower than this represents higher levels of organization [55]. Corresponding occurrence frequency histograms of the fitted  $\rho$  values for each image of the different tissues are shown in Fig. 2 panels c1-c6. It was assumed that a single population of collagen fibers exists within the tissues and therefore, the data was fitted with a single Gaussian function to obtain a mean  $\rho$  value. The mean  $\rho$  value from each image was obtained by averaging among all tissue scans to obtain an overall average  $\rho$  value for PDA, MDA and WDA tissues and their corresponding normal tissues, shown in Table 1. Similarly, the width of the fitted occurrence frequency histogram of the  $\rho$  values was obtained via the full-width at half-maximum of the Gaussian fit, and it was also averaged among all the tissues to obtain an average  $\rho$  distribution width, shown in Table 1.

The average  $\rho$  values of PDA and MDA tissues were found to be greater than the average  $\rho$  values of normal gastric tissues. Statistically significant differences were found between the average  $\rho$  values of PDA and MDA versus their normal counterparts (Fig. 3(a)) when using a two-tailed t-test and considering the total number of scans performed ( $p < 0.002$  and  $p < 0.01$ , respectively), however, a statistically significant difference was not observed when using patient averages to determine a mean value and considering the number of patients studied. The average  $\rho$  distribution width was significantly different between WDA and its normal counterpart ( $p < 0.05$ ) however, it was not significantly different between PDA and MDA versus their normal counterparts.

Additional analysis based on the  $\rho$  values found for each tissue type was also performed by finding the ratio of disordered pixels (RDP of  $\rho$ ) for each image, as described in section 2.3. Statistically significant differences were found between the RDP of  $\rho$  of PDA and MDA versus their normal counterparts when using a two-tailed t-test and considering the number of scans performed ( $p < 0.01$  and  $p < 0.01$ , respectively, Fig. 3(b)). A significant difference was also

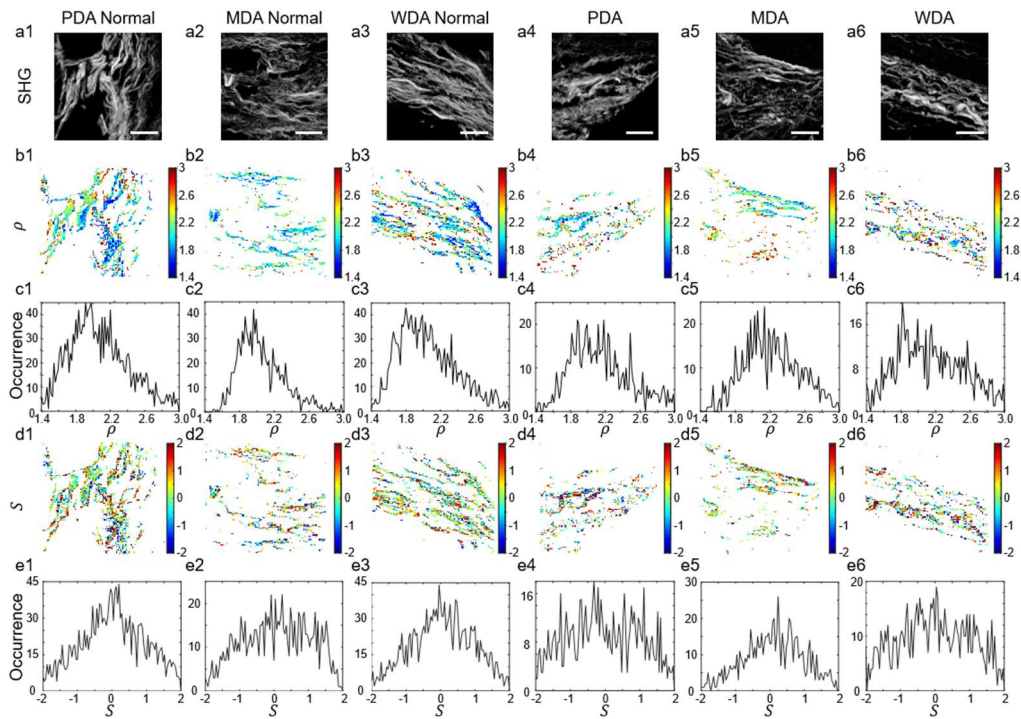


**Fig. 2.** PIPO SHG analysis of gastric tissue in patients diagnosed with adenocarcinoma. Normal gastric tissue from patients who were diagnosed with poorly differentiated adenocarcinoma (PDA, a1-e1), moderately differentiated adenocarcinoma (MDA, a2-e2) and well differentiated adenocarcinoma (WDA, a3-e3) as well as tumor tissue diagnosed as PDA (a4-e4), MDA (a5-e5) and WDA (a6-e6) from the same patients. Normalized SHG intensity images were produced by summing 64 polarization-dependent SHG intensity images and applying a logarithm (a1-a6). Color-coded maps of the fitted  $\rho$  values (b1 – b6) and occurrence frequency histograms of the  $\rho$  values (c1 – c6). Color-coded maps of the fitted  $S$  values (d1 – d6) and occurrence frequency histograms of the  $S$  values (e1 – e6). The scale bar in a1-a6 represents 25  $\mu\text{m}$ .

observed between the cancer classifications PDA versus WDA ( $p < 0.05$ ) as well as MDA versus WDA ( $p < 0.05$ ) when considering the number of scans taken.

Color-coded maps of the fitted  $\kappa$  values represent collagen polarity and indicate if the average tilt of the collagen fibers in the focal volume is above or below the imaging plane (Supplement 1 Fig. S3). The average values of  $|\kappa|$  for the adenocarcinoma tissues were not significantly different than their normal counterparts (see Table 1). However, a statistical difference was observed between the cancer classifications PDA versus MDA ( $p < 0.01$ ) as well as MDA versus WDA ( $p < 0.02$ ) when considering the number of scans taken. Significant differences were also observed in the average  $\kappa$  distribution widths of PDA versus its normal counterpart ( $p < 0.001$ ) as well as PDA versus WDA ( $p < 0.02$ ) when considering the number of scans taken.

Color-coded maps of calculated DOLP values for each pixel have been used in a previous study of thyroid tissue to visualize pixels with disordered collagen regions, such as due to small collagen fiber segments within the focal volume that may produce depolarized SHG signals [38]. However, in this study, the DOLP values of the adenocarcinoma tissues (Supplement 1 Fig. S3) were not significantly different than their normal counterparts and instead had relatively high DOLP values (Table 1).

**Table 1. PIPO SHG analysis summary for normal gastric tissue, PDA, MDA and WDA. The table contains the average  $\rho$  values, the distribution width of the  $\rho$  values, the ratio of disordered pixels (RDP of  $\rho$ ) with fitted  $\rho$  values between 2 and 3 per image to the total number of fitted pixels per image, the  $\kappa$  values, the distribution width of the  $\kappa$  values, the DOLP values, the  $|S|$  values and the full-width half-maximum values of the occurrence frequency histograms of  $S$  values. For all parameters the standard error is shown.**

Tissue	$\rho$	$\rho$ Width	RDP of $\rho$	$ \kappa $	$\kappa$ Width	DOLP	$ S $	$S$ Width
Normal from PDA	$2.03 \pm 0.02$	$0.52 \pm 0.01$	$0.54 \pm 0.01$	$0.0103 \pm 0.0009$	$0.083 \pm 0.002$	$0.889 \pm 0.004$	$0.064 \pm 0.006$	$1.49 \pm 0.03$
Normal from MDA	$2.00 \pm 0.02$	$0.50 \pm 0.02$	$0.52 \pm 0.02$	$0.015 \pm 0.002$	$0.085 \pm 0.004$	$0.897 \pm 0.005$	$0.053 \pm 0.08$	$1.55 \pm 0.04$
Normal from WDA	$2.03 \pm 0.02$	$0.56 \pm 0.02$	$0.54 \pm 0.02$	$0.012 \pm 0.001$	$0.087 \pm 0.003$	$0.870 \pm 0.008$	$0.058 \pm 0.008$	$1.45 \pm 0.04$
Total Normal	$2.02 \pm 0.01$	$0.53 \pm 0.01$	$0.538 \pm 0.009$	$0.0117 \pm 0.0007$	$0.084 \pm 0.002$	$0.886 \pm 0.003$	$0.062 \pm 0.005$	$1.49 \pm 0.02$
PDA	$2.09 \pm 0.02$	$0.53 \pm 0.02$	$0.60 \pm 0.01$	$0.012 \pm 0.001$	$0.096 \pm 0.003$	$0.882 \pm 0.004$	$0.096 \pm 0.007$	$1.61 \pm 0.03$
MDA	$2.11 \pm 0.03$	$0.50 \pm 0.03$	$0.61 \pm 0.03$	$0.020 \pm 0.003$	$0.093 \pm 0.005$	$0.897 \pm 0.005$	$0.13 \pm 0.02$	$1.53 \pm 0.05$
WDA	$2.03 \pm 0.03$	$0.48 \pm 0.03$	$0.53 \pm 0.03$	$0.012 \pm 0.002$	$0.084 \pm 0.004$	$0.86 \pm 0.03$	$0.11 \pm 0.02$	$1.66 \pm 0.05$
Total Cancer	$2.09 \pm 0.01$	$0.51 \pm 0.01$	$0.59 \pm 0.01$	$0.013 \pm 0.001$	$0.093 \pm 0.002$	$0.881 \pm 0.006$	$0.107 \pm 0.007$	$1.59 \pm 0.02$

Previous research has indicated that trigonal symmetry may be a better model, as compared to cylindrical, to distinguish normal and tumor regions via changes in the collagen structure in the ECM of breast tissue [25,26]. Since limited differences in the average parameters obtained using cylindrical symmetry were observed between gastric adenocarcinoma tissues and their corresponding normal tissues, fitting using trigonal symmetry (Eq. (2)) was applied allowing the trigonal parameter,  $S$ , to be extracted. It was observed that fitting the data with the trigonal symmetry equation resulted in fitting an extra 3-7% of pixels per image, while keeping the adjusted  $R^2 \geq 0.8$ , which was similar for normal and cancerous samples. Color-coded maps of the fitted  $S$  values are visualized (Fig. 2 panels d1-d6) along with occurrence frequency histograms of the fitted  $S$  values (Fig. 2 panels e1-e6) for each typical tissue image. The  $S$  occurrence frequency histograms were fitted with a single Gaussian function to obtain the mean  $S$  value. The absolute value of the mean  $S$  for each scan was subsequently averaged among several tissue scans to obtain an overall average  $|S|$  for the gastric adenocarcinoma tissues and corresponding normal gastric tissues. Statistically significant differences (Fig. 3(c)) were found between the average  $|S|$  values of PDA, MDA and WDA versus their normal counterparts when using a two-tailed t-test and considering the number of scans performed ( $p < 0.002$ ,  $p < 0.002$ , and  $p < 0.01$ , respectively).

The width of the fitted occurrence frequency histograms of  $S$  for each scan was also averaged among the tissues to obtain an average  $S$  distribution width. The average  $S$  distribution width of PDA and WDA (Fig. 3(d)) were found to be significantly greater than the average  $S$  distribution width of their corresponding normal tissues ( $p < 0.01$  and  $p < 0.01$ , respectively).

Due to the significant differences observed between the average  $|S|$  values for all the gastric adenocarcinoma tissues and their corresponding normal gastric tissues, numerical simulations were performed to understand the meaning of the  $S$  parameter in comparison to the  $\rho$  parameter.

An earlier interpretation of asymmetry ( $|A| = \left| \frac{\chi_{xxx}^{(2)} + \chi_{yzz}^{(2)}}{\chi_{zzz}^{(2)} + \chi_{zxx}^{(2)}} \right|$ ) which is related to the  $S$  parameter

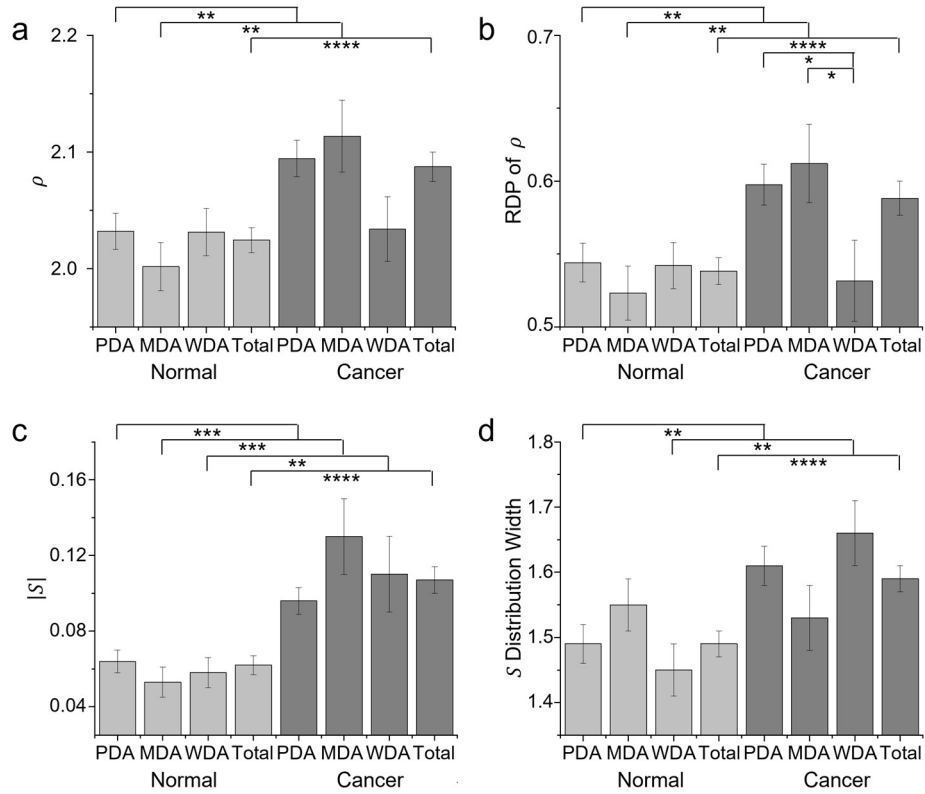


**Fig. 3.** Bar graphs of the  $\rho$  values (a), the ratio of disordered pixels (RDP of  $\rho$ ) with fitted  $\rho$  values between 2 and 3 per image to the total number of fitted pixels per image (b), the  $|S|$  values (c), and distribution width of the  $S$  values (d). The asterisks \*, \*\*, \*\*\* and \*\*\*\* indicate  $p < 0.05$ ,  $p < 0.01$ ,  $p < 0.002$  and  $p < 0.001$  significance, respectively.

indicated that an asymmetric distribution of collagen fibrils occurs ( $|A| > 0$ ) when two collagen fibrils of differing diameters intersect at an angle [56]. Therefore, numerical simulations of two intersecting collagen fibrils were performed at differing angles to one another and differing diameters to better understand the  $S$  parameter.

Numerical simulations showed that the  $\rho$  value resulting from two adjacent crossing cylindrically symmetric structures increases with angle (Fig. 4(a)). Furthermore, the  $\rho$  values increase similarly for three instances: (i) when the two cylindrical structures have the same diameter and the same  $\chi^{(2)}$  (see also Supplement 1 Fig. S6), (ii) when they have differing diameters and the same  $\chi^{(2)}$  (see also Supplement 1 Fig. S7), and (iii) when they have the same diameter and differing  $\chi^{(2)}$ . However, the  $|S|$  value of intersecting collagen fibrils only increases when the collagen fibrils are of different diameters (ii) or have different  $\chi^{(2)}$  values (iii). If the collagen fibrils have the same diameter and the same  $\chi^{(2)}$ , their  $|S|$  value remains low (Fig. 4(b)). Therefore, the modelling indicates that intersecting collagen fibrils of different diameters or  $\chi^{(2)}$  values results in  $|S|$  values further from zero. Up to now fibrils with different  $\chi^{(2)}$  values within the same tissue types have not been observed, therefore we attribute the increased  $|S|$  parameter to more intersecting fibrils of different diameters. Note that the  $|S|$  parameter versus angle of crossing (blue, solid in

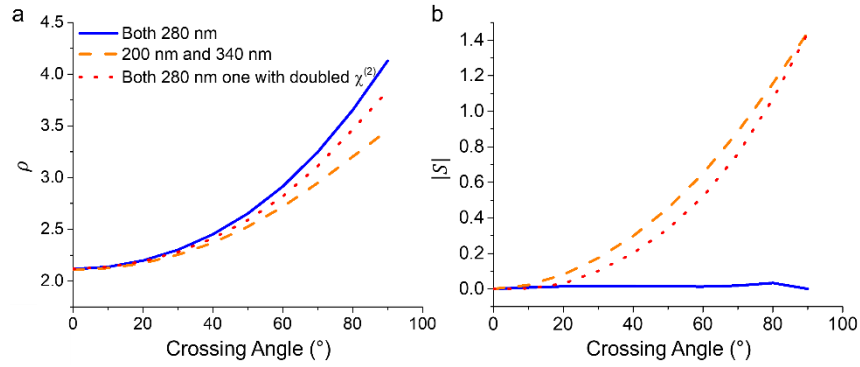


**Fig. 4.** Numerically simulated PIPO SHG datasets fitted with Eq. (2), revealing  $\rho$  (a) and  $|S|$  (b) values of intersecting cylindrically symmetric structures vs the angle between the two structures. Graphs (a) and (b) depict two cylindrically symmetric structures with the same (280 nm) diameter and the same  $\chi^{(2)}$  (blue, solid line), different diameters (280 nm and 340 nm) and the same  $\chi^{(2)}$  (orange, long dash), and with the same diameters (280 nm) but one with doubled  $\chi^{(2)}$  compared to the first (red, dash).

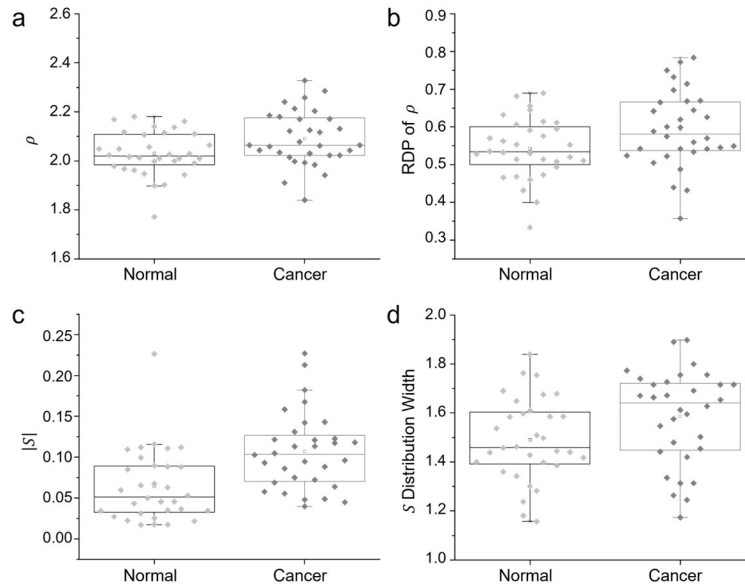


**Fig. 5.** A comparison of box plots of averaged PSHG parameters for each patient, representing their normal and cancerous stomach tissue. Parameter  $\rho$  is shown in (a), the ratio of the disordered pixels (RDP of  $\rho$ ) with fitted  $\rho$  values between 2 and 3 per image to the total number of fitted pixels per image (b), the  $|S|$  values (c), and the distribution width of the  $S$  values (d).

Fig. 4(b)) curve shows that fibrils with identical diameters have  $|S|$  which oscillates, having a slight maximum near  $20^\circ$  and  $80^\circ$ , and minimum near  $40^\circ$  and  $90^\circ$  (see Supplement 1 Fig. S6c).

Paired t-tests were evaluated to determine if a trend is observed between each individual's cancerous tissue and their normal tissue for the parameters  $\rho$ , RDP of  $\rho$ ,  $|S|$ , and  $S$  distribution

width. A statistically significant increase ( $p < 0.02$ ) of 0.06 on average in the  $\rho$  value was found between each patient's normal and cancerous tissue (Fig. 5(a)). A significant increase ( $p < 0.05$ ) was also found in the RDP of  $\rho$  values with an average increase of 0.05 when comparing each patient's normal and cancerous stomach tissue (Fig. 5(b)). With respect to the  $S$  values, a significant increase ( $p < 0.01$ ) in the  $|S|$  value was found, with an average increase of 0.02, in each patient's normal versus cancerous stomach tissue (Fig. 5(c)). The  $S$  distribution width increase is also statistically significant ( $p < 0.05$ ) having an average difference of 0.095 between normal and cancerous stomach tissue. Therefore, the parameters  $\rho$ , RDP of  $\rho$ ,  $|S|$  and the  $S$  distribution width all show a significant difference for each patient's cancerous stomach tissue when comparing between normal tissue.

## 4. Discussion

### 4.1. $\rho$ values

The statistically significant increase in  $\rho$  observed for tissues with PDA and MDA as compared to their normal counterparts is similar to previously reported variations in  $\rho$  between normal and tumor tissues in human lung [19,39], breast [27,33], thyroid [36,38], pancreas [37] and bone [43], indicative of increased collagen structural disorder with cancer. Furthermore, a paired t-test indicated that on average a patient's  $\rho$  values increased when comparing their normal to cancerous tissue regions. The changes in  $\rho$  during tumorigenesis have been previously proposed to be attributed to differences in one or more of several parameters including: (i) The amino acid content of the triple helices in normal and cancerous tissue, (ii) the arrangement of the triple helices into fibrils and fibers, and (iii) the distribution of fibrils and fibers within the laser focal volume [21]. Additionally, it should be noted that while the  $\rho$  variations between the different tissues in this study are presumed valid since they were all prepared the same way, the  $\rho$  values measured in this study are likely shifted from their *in situ* values due to dehydration during sample preparation, since in individual collagen fibrils dehydration raised  $\rho$  from 1.4 to 2.0 (see supporting S1 in [50]).

A significant difference was also observed in the RDP of  $\rho$  for tissues with PDA and MDA as compared to their normal counterparts. The color-coded maps of the  $\rho$  values of cancerous tissue appear to have more red pixels than the color-coded maps of the  $\rho$  values of the normal tissue (compare Fig. 2 panels b1-b3 versus b4-b6) and therefore, RDP of  $\rho$  was measured to see if there are significantly more disordered pixels ( $2 < \rho < 3$ ) in cancerous stomach tissue than normal tissue. This was found to be true amongst PDA and MDA tissues in comparison with their normal tissues, similar to the results obtained considering the average  $\rho$  values. Therefore, the RDP of  $\rho$  is a similar metric for discriminating cancerous tissue from normal tissue.

### 4.2. $\kappa$ values

Variations in the  $\kappa$  values occur based on collagen chirality and are modulated by tilt above or below the image plane [46]. Many of the pixels in color-coded maps of the  $\kappa$  values (Supplement 1 Fig. S3) correspond to 0 or they are clustered into small positive and negative polarity regions similarly in both the cancerous and normal tissues, hence, a significant difference was not observed in the average  $|\kappa|$  values between normal and cancerous tissues. However, a significant difference was observed in the distribution width of the  $\kappa$  values for PDA tissue indicating structural variations in the collagen fibers of cancerous tissue. The distribution widths of the occurrence frequency histograms of the  $\kappa$  values are attributed to the distribution of the out of image-plane tilt angles of collagen fibers, since variations in collagen chirality have not been reported in tissues, although they could occur. Here, the distribution width of the  $\kappa$  values for the cancerous tissues were generally larger than their normal counterparts similar to observations

made of the distribution width of the occurrence frequency histograms of the  $\kappa$  values for cancerous pancreatic tissue in comparison to normal parenchymal pancreatic tissue [37].

#### 4.3. DOLP values

A significant difference was not observed in the DOLP values or the distribution width of the DOLP values between cancerous and normal tissue. This is surprising because the DOLP has been previously observed to be markedly different between tissues with thyroid diseases [36,38] and normal tissues as well as pancreatic ductal adenocarcinoma [37] and normal tissues, and may indicate that gastric adenocarcinoma does not misalign collagen to the same extent as in the pancreas or thyroid. Zhou et al. previously performed SHG imaging of gastric cancer and investigated several architectural parameters including alignment, density, width, length and straightness [57]. They found that all these parameters were significantly increased in the tumor microenvironment indicating that cancerous tissue may be more aligned with gastric cancer [57]. The increased alignment of the macroscale arrangement of collagen in gastric cancer may lead to high DOLP values, hence, increased  $\rho$  values found in this paper are indicative of increased disorder related to the nanoscale arrangement of collagen in gastric cancer.

#### 4.4. $S$ values

In addition to cylindrical symmetry, trigonal symmetry was explored as another measurement of disordered collagen fibers in cancerous tissue by fitting the  $S$  parameter. Trigonal symmetry was found to fit approximately the same number of pixels as those fit with cylindrical symmetry for all the tissues while keeping the adjusted  $R^2 \geq 0.8$  and also had similar  $R^2$  values to fits with cylindrical symmetry. Therefore, fitting with trigonal symmetry may be potentially as useful as cylindrical symmetry. The  $S$  parameter can be used to monitor the balance between cylindrical ( $S = 0$ ) and trigonal symmetries ( $|S| > 0$ ). Furthermore, the  $S$  value is typically centered around zero and may have an average positive or negative value like the  $\kappa$  value, hence, the absolute value of the mean of  $S$  was obtained for each scan, similar to previous measurements made using trigonal symmetry [25].

It has been suggested that trigonal symmetry may occur due to a helicoidal or cholesteric collagen ultrastructure [26,58]. It has also been implied by measurement of an asymmetry term that trigonal symmetry may occur due to intersecting collagen fibrils of differing diameters at an angle [56]. From our simulations shown in Fig. 4(b), we found that  $|S| > 0$  when two intersecting collagen fibrils have differing diameters or differing  $\chi^{(2)}$  values, but unlike  $\rho$ ,  $S$  does not significantly change when fibrils that intersect have the same diameters and  $\chi^{(2)}$ , except for small oscillations discussed in section 3. Therefore, under the assumption that all fibrils have the same  $\chi^{(2)}$ , the statistically significant increase in the  $|S|$  parameter of PDA, MDA and WDA as compared to their corresponding normal tissues suggests that PDA, MDA and WDA tissues may be due to more intersecting collagen fibrils of varying diameters than their corresponding normal tissues. An increase in the  $\rho$  values is also expected for this instance and a statistically significant difference is seen for PDA and MDA versus their corresponding normal tissue. However, a statistically significant difference in the  $\rho$  values of WDA and its corresponding normal tissue was not observed. According to Fig. 4(a) and (b), this may indicate that the angle at which the collagen fibrils are intersecting in WDA is not as large ( $\sim 20^\circ$ ) where the  $\rho$  values do not appreciably change, but differences in  $|S|$  are seen. It should also be noted though that the  $|S|$  value is smallest in WDA. This may be expected from previous observations of picrosirius red stained oral squamous cell carcinoma tissues with a polarizing microscope which found that in well differentiated tumor microenvironments, the collagen fibers present in the tissue were oriented in a parallel arrangement, but in poorly differentiated tumor microenvironments, collagen fibers were found to be arranged haphazardly and had an increased amount of thinner

collagen fibers [59,60]. Therefore,  $|S|$  may be a measure of disorder in cancerous tissue amongst intersecting collagen fibrils of differing diameters.

Increased  $|S|$  values were also previously observed in malignant breast tissues as compared to their normal counterparts [25]. Although a significant variation between the cancerous tissues themselves is not observed with  $|S|$ , it is exciting to find that a single parameter that is able to distinguish all three gastric cancer types from normal tissue. Furthermore, a paired t-test showed that on average patient's  $|S|$  values significantly increased when comparing their normal and cancerous tissue regions.

A statistically significant difference was also observed in the distribution width of the  $S$  values for tissues with PDA and WDA as compared to their normal counterparts. In general, the distribution widths of the  $S$  values of the cancerous tissues were significantly larger than the distribution width of the  $S$  values of the normal tissues indicating that there is greater heterogeneity found with this parameter in cancerous tissue, similar to previous observations made with normal and malignant breast tissue [25]. It was additionally found via paired t-test that on average, a patient's  $S$  distribution width had a statistically significant increase in their cancerous tissue as compared to normal tissue adjacent to their cancerous tissue.

## 5. Conclusions

Human gastric adenocarcinoma tissues with three levels of cell differentiation were investigated by PSHG. The PSHG parameters obtained assuming cylindrical symmetry including  $\rho$  and the ratio of disordered pixels as determined by a specific range of  $\rho$  values were found to distinguish PDA and MDA from their normal tissues while the distribution width of the  $\kappa$  values was found to distinguish PDA and WDA from their normal tissues. Trigonal symmetry was additionally applied and the PSHG parameter,  $|S|$ , was found to distinguish all three levels of cell differentiation, PDA, MDA and WDA, from their normal tissues while the distribution width of the  $S$  values was found to distinguish PDA and WDA from their normal tissues. Further analysis of average variation in parameters of individual patients demonstrated that the  $\rho$  values, the ratio of disordered pixels of  $\rho$  values, the  $|S|$  values and the distribution width of the  $S$  values of their cancerous tissue had statistically significant differences compared to normal tissue. And in light of previous work [57], this indicates increased disorder at the nano (sub-fiber) scale. Furthermore, analysis of numerical simulations revealed that an increase in the  $|S|$  parameter likely occurs due to more intersecting collagen fibrils of varying diameters. In summary, the results indicate that of the parameters investigated,  $|S|$  is the most promising candidate for differentiating between cancerous and normal tissue for gastric adenocarcinoma and may be applied for automated pathology.

**Funding.** Natural Sciences and Engineering Research Council of Canada (Discovery Grants Program RGPIN-2018-05444); Canada Foundation for Innovation (John R. Evans Leaders Fund #37749); Research Nova Scotia (1868); Canada's Research Support Fund; Saint Mary's University.

**Acknowledgments.** The authors would like to thank Dr. David Dansereau (Department of Biology, Saint Mary's University) for suggestions on data analysis and statistical tests.

**Disclosures.** The authors declare that there are no conflicts of interest related to this article.

**Data Availability.** Data underlying the results presented in this paper are available in [Supplement 1](#).

**Supplemental document.** See [Supplement 1](#) for supporting content.

## References

1. P. Rawla and A. Barsouk, "Epidemiology of gastric cancer: Global trends, risk factors and prevention," *Prz Gastroenterol* **14**(1), 26–38 (2019).
2. E. Morgan, M. Arnold, M. Constanza Camargo, A. Gini, A. T. Kunzmann, T. Matsuda, F. Meheus, R. H. A. Verhoeven, J. Vignat, M. Laversanne, J. Ferlay, and I. Soerjomataram, "The current and future incidence and mortality of gastric cancer in 185 countries, 2020–40: A population-based modelling study," (2022).
3. R. Sitarz, M. Skierucha, J. Mielko, G. J. A. Offerhaus, R. Maciejewski, and W. P. Polkowski, "Gastric cancer: Epidemiology, prevention, classification, and treatment," *Cancer Manag. Res.* **10**, 239–248 (2018).

4. G. Schwartz, "Invasion and metastases in gastric cancer: in vitro and in vivo models with clinical correlations," *Semin. Oncol.* **23**(3), 316–324 (1996).
5. A. Jögi, M. Vaapil, M. Johansson, and S. Pählman, "Cancer cell differentiation heterogeneity and aggressive behavior in solid tumors," *Ups J. Med. Sci.* **117**(2), 217–224 (2012).
6. M. Joo and S. H. Han, "Gastric-type extremely well-differentiated adenocarcinoma of the stomach: A challenge for preoperative diagnosis," *J. Pathol. Transl. Med.* **50**(1), 71–74 (2016).
7. T. Arai, Y. Matsuda, J. Aida, K. Takubo, and T. Ishiwata, "Solid-type poorly differentiated adenocarcinoma of the stomach: clinicopathological and molecular characteristics and histogenesis," *Gastric Cancer* **22**(2), 314–322 (2019).
8. S. S. Joshi and B. D. Badgwell, "Current treatment and recent progress in gastric cancer," *CA Cancer J. Clin.* **71**(3), 264–279 (2021).
9. T. Guszczyn and K. Sobolewski, "Deregulation of collagen metabolism in human stomach cancer," *Pathobiology* **71**(6), 308–313 (2004).
10. C. Frantz, K. M. Stewart, and V. M. Weaver, "The extracellular matrix at a glance," *J. Cell Sci.* **123**(24), 4195–4200 (2010).
11. A. M. Moreira, J. Pereira, S. Melo, M. S. Fernandes, P. Carneiro, R. Seruca, and J. Figueiredo, "The extracellular matrix: an accomplice in gastric cancer development and progression," *Cells* **9**(2), 394 (2020).
12. S. Roth and I. Freund, "Second harmonic generation in collagen," *J. Chem. Phys.* **70**(4), 1637–1643 (1979).
13. G. Hall, K. W. Eliceiri, and P. J. Campagnola, "Simultaneous determination of the second-harmonic generation emission directionality and reduced scattering coefficient from three-dimensional imaging of thick tissues," *J. Biomed. Opt.* **18**(11), 116008 (2013).
14. R. LaComb, O. Nadiarnykh, S. Carey, and P. J. Campagnola, "Quantitative second harmonic generation imaging and modeling of the optical clearing mechanism in striated muscle and tendon," *J. Biomed. Opt.* **13**(2), 021109 (2008).
15. O. Nadiarnykh, R. B. LaComb, M. A. Brewer, and P. J. Campagnola, "Alterations of the extracellular matrix in ovarian cancer studied by Second Harmonic Generation imaging microscopy," *BMC Cancer* **10**(1), 94 (2010).
16. F. J. Ávila and J. M. Bueno, "Analysis and quantification of collagen organization with the structure tensor in second harmonic microscopy images of ocular tissues," *Appl. Opt.* **54**(33), 9848–9854 (2015).
17. J. M. Bueno, F. J. Ávila, and M. C. Martínez-García, "Quantitative analysis of the corneal collagen distribution after in vivo cross-linking with second harmonic microscopy," *Biomed. Res. Int.* **2019**, 1–12 (2019).
18. K. L. Gant, A. N. Jambor, Z. Li, E. C. Rentchler, P. Weisman, L. Li, M. S. Patankar, and P. J. Campagnola, "Evaluation of collagen alterations in early precursor lesions of high grade serous ovarian cancer by second harmonic generation microscopy and mass spectrometry," *Cancer* **13**(11), 2794 (2021).
19. A. Golaraei, L. B. Mostaço-Guidolin, V. Raja, R. Navab, T. Wang, S. Sakashita, K. Yasufuku, M.-S. Tsao, B. C. Wilson, and V. Barzda, "Polarimetric second-harmonic generation microscopy of the hierarchical structure of collagen in stage I-III non-small cell lung carcinoma," *Biomed. Opt. Express* **11**(4), 1851–1863 (2020).
20. L. B. Mostaço-Guidolin, E. T. Osei, J. Ullah, S. Hajimohammadi, M. Fouadi, X. Li, V. Li, F. Shaheen, C. X. Yang, F. Chu, D. J. Cole, C. A. Brandsma, I. H. Heijink, G. N. Maksym, D. Walker, and T. L. Hackett, "Defective fibrillar collagen organization by fibroblasts contributes to airway remodeling in asthma," *Am. J. Respir. Crit. Care Med.* **200**(4), 431–443 (2019).
21. D. Pouli, E. M. Genega, T. B. Sullivan, K. M. Rieger-Christ, V. Wright, I. Georgakoudi, and T. Schnellrdorfer, "Two-photon images reveal unique texture features for label-free identification of ovarian cancer peritoneal metastases," *Biomed. Opt. Express* **10**(9), 4479–4488 (2019).
22. J. M. Bueno, F. J. Ávila, R. Hristu, S. G. Stanciu, L. Eftimie, and G. A. Stanciu, "Objective analysis of collagen organization in thyroid nodule capsules using second harmonic generation microscopy images and the Hough transform," *Appl. Opt.* **59**(23), 6925–6931 (2020).
23. T. Hompland, A. Erikson, M. Lindgren, T. Lindmo, and C. de Lange Davies, "Second-harmonic generation in collagen as a potential cancer diagnostic parameter," *J. Biomed. Opt.* **13**(5), 054050 (2008).
24. D. Ait-Belkacem, A. Gasecka, F. Munhoz, S. Brustlein, and S. Brasselet, "Influence of birefringence on polarization resolved nonlinear microscopy and collagen SHG structural imaging," *Opt. Express* **18**(14), 14859–14870 (2010).
25. R. Ambekar, T.-Y. Lau, M. Walsh, R. Bhargava, and K. C. Toussaint, "Quantifying collagen structure in breast biopsies using second-harmonic generation imaging," *Biomed. Opt. Express* **3**(9), 2021–2035 (2012).
26. R. Mercatelli, T. Triulzi, F. S. Pavone, R. Orlandi, and R. Cicchi, "Collagen ultrastructural symmetry and its malignant alterations in human breast cancer revealed by polarization-resolved second-harmonic generation microscopy," *J. Biophotonics* **13**(8), e202000159 (2020).
27. V. Tsafas, E. Gavgiotaki, M. Tzardi, E. Tsafa, C. Fotakis, I. Athanassakis, and G. Filippidis, "Polarization-dependent second-harmonic generation for collagen-based differentiation of breast cancer samples," *J. Biophotonics* **13**(10), e202000180 (2020).
28. W. C. Chen, Y. J. Chen, S. T. Lin, W. H. Hung, M. C. Chan, I. C. Wu, M. T. Wu, C. T. Kuo, S. Das, F. J. Kao, and G. Y. Zhuo, "Label-free characterization of collagen fibers in cancerous esophagus tissues using ratiometric nonlinear optical microscopy," *Exp. Biol. Med.* **245**(14), 1213–1221 (2020).
29. F. Radaelli, L. D'Alfonso, M. Collini, F. Mingozzi, L. Marongiu, F. Granucci, I. Zanoni, G. Chirico, and L. Sironi, "µmAPPS: A novel phasor approach to second harmonic analysis for in vitro-in vivo investigation of collagen microstructure," *Sci. Rep.* **7**(1), 17468 (2017).

30. R. Scodellaro, M. Bouzin, and F. Mingozzi, *et al.*, "Whole-section tumor micro-architecture analysis by a two-dimensional phasor-based approach applied to polarization-dependent second harmonic imaging," *Front. Oncol.* **9**, 527 (2019).
31. K. R. Campbell, R. Chaudhary, J. M. Handel, M. S. Patankar, and P. J. Campagnola, "Polarization-resolved second harmonic generation imaging of human ovarian cancer," *J. Biomed. Opt.* **23**(6), 066501 (2018).
32. K. R. Campbell and P. J. Campagnola, "Assessing local stromal alterations in human ovarian cancer subtypes via second harmonic generation microscopy and analysis," *J. Biomed. Opt.* **22**(11), 116008 (2017).
33. A. Golaraei, L. Kontenis, R. Cisek, D. Tokarz, S. J. Done, B. C. Wilson, and V. Barzda, "Changes of collagen ultrastructure in breast cancer tissue determined by second-harmonic generation double stokes-mueller polarimetric microscopy," *Biomed. Opt. Express* **7**(10), 4054–4068 (2016).
34. X. Han, R. M. Burke, M. L. Zettel, P. Tang, and E. B. Brown, "Second harmonic properties of tumor collagen: determining the structural relationship between reactive stroma and healthy stroma," *Opt. Express* **16**(3), 1846–1859 (2008).
35. C. Doras, G. Taupier, A. Barsella, L. Mager, A. Boeglin, H. Bulou, P. Bousquet, and K. D. Dorkenoo, "Polarization state studies in second harmonic generation signals to trace atherosclerosis lesions," *Opt. Express* **19**(16), 15062–15068 (2011).
36. D. Tokarz, R. Cisek, A. Golaraei, S. L. Asa, V. Barzda, and B. C. Wilson, "Ultrastructural features of collagen in thyroid carcinoma tissue observed by polarization second harmonic generation microscopy," *Biomed. Opt. Express* **6**(9), 3475–3481 (2015).
37. D. Tokarz, R. Cisek, A. Joseph, A. Golaraei, K. Mirsanaye, S. Krouglov, S. L. Asa, B. C. Wilson, and V. Barzda, "Characterization of pancreatic cancer tissue using multiphoton excitation fluorescence and polarization-sensitive harmonic generation microscopy," *Front. Oncol.* **9**, 272 (2019).
38. D. Tokarz, R. Cisek, A. Joseph, S. L. Asa, B. C. Wilson, and V. Barzda, "Characterization of pathological thyroid tissue using polarization-sensitive second harmonic generation microscopy," *Lab. Invest.* **100**(10), 1280–1287 (2020).
39. A. Golaraei, R. Cisek, S. Krouglov, R. Navab, C. Niu, S. Sakashita, K. Yasufuku, M.-S. Tsao, B. C. Wilson, and V. Barzda, "Characterization of collagen in non-small cell lung carcinoma with second harmonic polarization microscopy," *Biomed. Opt. Express* **5**(10), 3562–3567 (2014).
40. R. Cisek, A. Joseph, M. Harvey, and D. Tokarz, "Polarization-sensitive second harmonic generation microscopy for investigations of diseased collagenous tissues," *Front. Phys.* **9**, 726996 (2021).
41. R. Cisek, M. Harvey, E. Bennett, H. Jeon, and D. Tokarz, "Polarization-resolved SHG microscopy for biomedical applications," in *Optical Polarimetric Modalities for Biomedical Research*, N. Mazumder, Y. V. Kistenev, E. Borisova, and S. P. Kabekkodu, eds., 1st ed. (Springer Nature Switzerland AG, 2023), Vol. 1, pp. 215–258.
42. C. Okoro, V. Kelkar, M. Sivaguru, R. Emmadi, and K. C. Toussaint, "Second-harmonic patterned polarization-analyzed reflection confocal microscopy of stromal collagen in benign and malignant breast tissues," *Sci. Rep.* **8**(1), 16243 (2018).
43. M. Burke, A. Golaraei, A. Atkins, M. Akens, V. Barzda, and C. Whyne, "Collagen fibril organization within rat vertebral bone modified with metastatic involvement," *J. Struct. Biol.* **199**(2), 153–164 (2017).
44. J. W. Birk, M. Tadros, K. Moezardalan, O. Nadyarnykh, F. Forouhar, J. Anderson, and P. Campagnola, "Second harmonic generation imaging distinguishes both high-grade dysplasia and cancer from normal colonic mucosa," *Dig. Dis. Sci.* **59**(7), 1529–1534 (2014).
45. F. Tiaho, G. Recher, and D. Rouède, "Estimation of helical angles of myosin and collagen by second harmonic generation imaging microscopy," *Opt. Express* **15**(19), 12286–12295 (2007).
46. A. Golaraei, K. Mirsanaye, Y. Ro, S. Krouglov, M. K. Akens, B. C. Wilson, and V. Barzda, "Collagen chirality and three-dimensional orientation studied with polarimetric second-harmonic generation microscopy," *J. Biophotonics* **12**(1), e201800241 (2019).
47. K. Brittain, M. Harvey, R. Cisek, S. Pillai, S. D. Christie, and D. Tokarz, "Second harmonic generation microscopy of otoconia," *Biomed. Opt. Express* **13**(6), 3593–3600 (2022).
48. A. E. Tuer, S. Krouglov, N. Prent, R. Cisek, D. Sandkuijl, K. Yasufuku, B. C. Wilson, and V. Barzda, "Nonlinear optical properties of type I collagen fibers studied by polarization dependent second harmonic generation microscopy," *J. Phys. Chem. B* **115**(44), 12759–12769 (2011).
49. C. A. Dailey, B. J. Burke, and G. J. Simpson, "The general failure of Kleinman symmetry in practical nonlinear optical applications," *Chem. Phys. Lett.* **390**(1-3), 8–13 (2004).
50. M. Harvey, R. Cisek, M. Alizadeh, V. Barzda, L. Kreplak, and D. Tokarz, "High numerical aperture imaging allows chirality measurement in individual collagen fibrils using polarization second harmonic generation microscopy," *Nanophotonics* **12**(11), 2061–2071 (2023).
51. E. Bennett, M. Harvey, R. Cisek, and D. Tokarz, "An investigation into the structure of crystalline maltodextrin particles by second harmonic generation microscopy," *Biomed. Opt. Express* **14**(3), 1027–1040 (2023).
52. A. E. Tuer, M. K. Akens, S. Krouglov, D. Sandkuijl, B. C. Wilson, C. M. Whyne, and V. Barzda, "Hierarchical model of fibrillar collagen organization for interpreting the second-order susceptibility tensors in biological tissue," *Biophys. J.* **103**(10), 2093–2105 (2012).
53. D. Sandkuijl, A. E. Tuer, D. Tokarz, J. E. Sipe, and V. Barzda, "Numerical second- and third-harmonic generation microscopy," *J. Opt. Soc. Am. B* **30**(2), 382–395 (2013).

54. R. LaComb, O. Nadiarnykh, S. S. Townsend, and P. J. Campagnola, "Phase matching considerations in second harmonic generation from tissues: Effects on emission directionality, conversion efficiency and observed morphology," *Opt. Commun.* **281**(7), 1823–1832 (2008).
55. G. J. Simpson and K. L. Rowlen, "An SHG magic angle: Dependence of second harmonic generation orientation measurements on the width of the orientation distribution," *J. Am. Chem. Soc.* **121**(11), 2635–2636 (1999).
56. A. E. Tuer, "Nonlinear Microscopy for Histology," (2013).
57. Z. H. Zhou, C. D. Ji, H. L. Xiao, H. Bin Zhao, Y. H. Cui, and X. W. Bian, "Reorganized collagen in the tumor microenvironment of gastric cancer and its association with prognosis," *J. Cancer* **8**(8), 1466–1476 (2017).
58. R. Mercatelli, S. Mattana, L. Capozzoli, F. Ratto, F. Rossi, R. Pini, D. Fioretto, F. S. Pavone, S. Caponi, and R. Cicchi, "Morpho-mechanics of human collagen superstructures revealed by all-optical correlative micro-spectroscopies," *Commun. Biol.* **2**(1), 117 (2019).
59. P. Kardam, M. Mehendiratta, S. Rehani, M. Kumra, K. Sahay, and K. Jain, "Stromal fibers in oral squamous cell carcinoma: A possible new prognostic indicator?" *J. Oral Maxillofacial Pathol.* **20**(3), 405–412 (2016).
60. B. Bordoloi, S. Siddiqui, R. Jaiswal, A. Tandon, A. Jain, and R. Chaturvedi, "A quantitative and qualitative comparative analysis of collagen fibers to determine the role of connective tissue stroma in oral squamous cell carcinoma using special stains and polarized microscopy," *J. Oral Maxillofacial Pathol.* **24**(2), 398 (2020).